Spectroscopic Studies of Cyclo-metallated Pt(II) Complexes: Spectroscopic Evidence of Strong Inter-complex Coupling in Single Crystal $[Pt(bpm)(CN)_2]\cdot DMF$ (bpm = 2,2′-bipyrimidine)

JOSEF BIEDERMANN, GÜNTER GLIEMANN*

Institut für Physikalische und Theoretische Chemie, Universität Regensburg, D-8400 Regensburg (F.R.G.)

ULRICH KLEMENT, KLAUS-JÜRGEN RANGE* and MANFRED ZABEL

Institut für Anorganische Chemie, Universität Regensburg, D-8400 Regensburg (F.R.G.)

(Received August 25, 1989)

Abstract

The optical properties (polarized absorption and emission) of single crystal $[Pt(bpm)(CN)_2]\cdot DMF$ under variation of temperature ($1.9\ K \leqslant T \leqslant 295\ K$) and homogeneous magnetic fields ($0 \leqslant H \leqslant 6$ T) are reported. When the magnetic field strength is raised from $H = 0$ to 6 T, the low-temperature emission is blue shifted by 220 cm^{-1}, the intensity increases by a factor of ~27, and the lifetime is reduced from $\tau = 1.8$ ms to 15 μs. The spectroscopic results are explained on the basis of the crystal structure of $[Pt(bpm)(CN)_2]\cdot DMF$, which exhibits columns of $[Pt(bpm)(CN)_2]$ complexes with a nearly face-to-face arrangement and relatively short Pt–Pt distances (~3.28 Å), yielding a distinct inter-complex coupling. Crystallographic data for $[Pt(bpm)(CN)_2]\cdot DMF$: monoclinic, space group $P2_1/m$, $a = 10.702(2)$, $b = 6.518(1)$, $c = 10.700(2)$ Å, $\beta = 95.57(2)°$, $V = 742.86$ Å^3, $Z = 2$, $D_c = 2.14$ g cm^{-3}, μ(Mo Kα) = 95.5 cm^{-1}, $R = 0.069$, $R_w = 0.056$ for 113 variables and 3497 reflexes with $I > 3\sigma(I)$.

Introduction

Many planar d^8 complexes tend to form quasi-one-dimensional structures in the crystalline state. An example are the comprehensively studied tetracyanoplatinates(II) [1, 2]. The square planar $[Pt(CN)_4]^{2-}$ units are stacked in columns. The intra-columnar Pt–Pt distance is short compared to the separation from column to column, resulting in a strongly anisotropic interaction between the complex ions. These compounds represent semiconductors with band gaps lying in the optical energy range, and they show characteristic magneto-optical effects [3–5]. A similar behavior has been found also for several platinum(II) complexes with large organic ligands such as $[Pt(bipy)(CN)_2]$ [6] and $[Pt(o\text{-phen})(CN)_2]$ [7]. For other cyclo-metallated complexes without CN^- ligands, e.g. for $[Pt(o\text{-phen})(en)]Cl_2$ [8], completely different magneto-optical properties are observed, indicating an imperceptible inter-complex coupling.

The compound $[Pt(bpm)(CN)_2]$ exhibits an outstanding feature. Depending on the conditions of crystallization different crystal modifications result [9]. As has been shown recently, single crystal $[Pt(bpm)(CN)_2]\cdot H_2O$ behaves spectroscopically like $[Pt(o\text{-phen})(en)]Cl_2$ [8]. The title compound $[Pt(bpm)(CN)_2]\cdot DMF$, however, indicates optical properties, which resemble those of the tetracyanoplatinates(II). The purpose of this paper is to describe these properties and to correlate them with the crystal structure.

Experimental

$[Pt(bpm)(CN)_2]\cdot DMF$ was prepared from a solution of 20 mg $[Pt(bpm)(CN)_2]\cdot H_2O$, cf. ref. 9, in 100 ml heated DMF. By slow evaporation of the solvent at 30 °C red needle shaped crystals grow, which decompose at humidity to $[Pt(bpm)(CN)_2]\cdot 1.5H_2O$. To preserve the crystals from decomposition they were covered by a thin film of paraffin. *Anal.* Found: C, 32.7; H, 2.7; N, 20.6. Calc.: C, 32.6; H, 2.7; N, 20.5%. For the spectroscopic measurements single crystals of a size of about 2 × 0.5 × 0.2 mm were used.

The apparatus used for the spectroscopic measurements at different temperatures and under magnetic fields was described in refs. 4 and 10.

Most of the crystals obtained by the evaporation method were of poor quality, perhaps due to the onset of decomposition. After inspection of a large number by X-ray film methods and optical microscopy a crystal fragment (approx. dimension 0.06 × 0.08 × 0.24 mm) could be found which was suitable

*Authors to whom correspondence should be addressed.

0020-1693/90/$3.50

for data collection on an Enraf-Nonius CAD-4 diffractometer (Mo Kα, $\lambda = 0.71073$ Å; graphite monochromator in incident beam). Lattice parameters were refined from 2θ values of 25 reflections in the range $10 \leqslant \theta \leqslant 14°$. Intensities were measured for $2 \leqslant \theta \leqslant 35°$ in an ω–2θ scan technique, scan width $(0.7 + 0.34 \tan \theta)°$. ψ-scans showed serious absorption effects. Three standard reflections showed an intensity loss of 1.6% throughout data collection. Merging of the 6813 collected intensities ($\sin\theta_{max}/\lambda = 0.81$ Å^{-1}; $-17 \leqslant h \leqslant 17$, $-10 \leqslant k \leqslant 10$, $0 \leqslant l \leqslant 17$) gave 3497 unique reflections with $I > 3\sigma(I)$ ($R_{int} = 0.026$) which were considered as observed and used for all subsequent calculations.

The structure was solved by Patterson and direct methods using the program SHELXS-86, followed by successive Fourier and difference Fourier syntheses (program system SDP 3.1; Enraf-Nonius). In full-matrix least-squares refinement $|F|$ magnitudes were used to refine atomic coordinates and isotropic temperature factors of the non-hydrogen atoms. After convergence at $R_w = 0.070$ (64 variables) a numerical correction for absorption was applied (program DIFABS; $T_{min} = 0.83$, $T_{max} = 1.0$). Residuals after final refinement cycle (isotropic for the DMF atoms, anisotropic for all other non-hydrogen atoms, 113 variables) $R = 0.069$, $R_w = 0.056$, $w = 4I/(\sigma^2(I) + 0.04^2I^2)$, $S = 1.3$. Max. features in the final Δ_ρ map + 3.7, −2.9 e Å^{-3}.

The position of the DMF molecule in the unit cell is not well defined. Only the carbon and nitrogen atoms could be localized and (isotropically) refined. For the purpose of the present paper, however, this is not of great importance.

[Pt(bmp)(CN)$_2$]·DMF exhibits a strong pseudo-symmetry. From the metrical relations of the reduced cell a monoclinic P cell (space group $P2_1/m$) as well as an orthorhombic cell can be deduced. The latter is C-centered, probable space group *Cmcm* (a minimal supergroup of $P2_1/m$). Refinement in *Cmcm*, however, was not successful (poor convergence, higher e.s.d.s, higher R values than in $P2_1/m$). This situation may of course result from the rather poor quality of the available intensity data and insufficient absorption correction. As long as the true space group of the compound has not been determined unequivocally, we prefer the description of the structural data in $P2_1/m$.

Results

Structure

The unit cell of [Pt(bpm)(CN)$_2$]·DMF is shown in Fig. 1, the corresponding cell parameters are summarized in Table 1. In Tables 2–4 positional parameters, interatomic distances (Å), and bond angles (°), respectively, are given. The numbering scheme of the

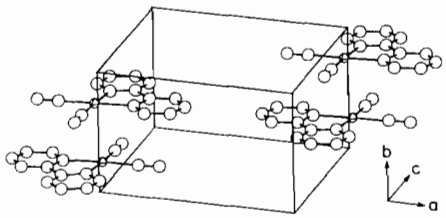

Fig. 1. ORTEP plot of the complexes [Pt(bpm)(CN)$_2$] in the [Pt(bpm)(CN)$_2$]·DMF crystal. DMF molecules omitted.

TABLE 1. Crystal data for [Pt(bpm)(CN)$_2$]·DMF

M_r	478.38
Space group	$P2_1/m$
a (Å)	10.702(2)
b (Å)	6.518(1)
c (Å)	10.700(2)
α (°)	90
β (°)	95.57(2)
γ (°)	90
V (Å^3)	742.86
Z	2
D_x (g cm^{-3})	2.14
μ(Mo Kα) (cm^{-1})	95.5
R	0.069
R_w	0.056

TABLE 2. Positional parameters and their e.s.d.s for [Pt(bpm)(CN)$_2$]·DMF

Atom	x	y	z	B (Å^2)[a]
Pt	0.01414(3)	0.250	0.01396(3)	1.988(4)
N1	0.3019(9)	0.250	0.034(1)	6.1(3)
N2	0.033(1)	0.250	0.3040(9)	6.5(3)
N3	0.509(2)	0.250	0.342(2)	11.7(6)*
N11	−0.0125(8)	0.250	−0.1776(7)	2.9(1)
N12	−0.167(1)	0.250	−0.348(1)	6.7(3)
N21	−0.1787(7)	0.250	−0.0148(9)	3.2(2)
N22	−0.350(1)	0.250	−0.168(1)	7.7(3)
C1	0.1957(9)	0.250	0.025(1)	3.8(2)
C2	0.028(1)	0.250	0.194(1)	4.0(2)
C3	0.355(2)	0.250	0.362(2)	7.1(4)*
C4	0.668(2)	0.505(3)	0.330(2)	5.2(4)*
C11	−0.128(1)	0.250	−0.228(1)	4.4(2)
C12	−0.081(3)	0.250	−0.424(1)	11.7(8)
C13	0.043(2)	0.250	−0.384(1)	8.8(5)
C14	0.075(1)	0.250	−0.259(1)	5.4(3)
C21	−0.225(1)	0.250	−0.133(1)	4.3(2)
C22	−0.426(1)	0.250	−0.068(3)	12.3(9)
C23	−0.383(1)	0.250	0.045(2)	8.7(5)
C24	−0.2584(9)	0.250	0.079(1)	5.1(3)

[a]Starred atoms were refined isotropically. Anisotropically refined atoms are given in the form of the isotropic equivalent thermal parameter defined as: $4/3[a^2B(1,1) + b^2B(2,2) + c^2B(3,3) + ab\cos\gamma B(1,2) + ac\cos\beta B(1,3) + bc\cos\alpha B(2,3)]$.

TABLE 3. Selected bond distances (Å) for [Pt(bpm)(CN)$_2$]·DMF [a]

Atom 1	Atom 2	Distance
Pt	C1	1.935(9)
Pt	C2	1.92(1)
Pt	N11	2.042(8)
Pt	N21	2.057(7)
C1	N1	1.13(1)
C2	N2	1.17(1)
N11	C11	1.30(1)
N11	C14	1.34(1)
C14	C13	1.35(2)
C13	C12	1.35(3)
N12	C12	1.29(3)
N12	C11	1.31(2)
N21	C21	1.31(1)
N21	C24	1.38(1)
C24	C23	1.35(1)
C23	C22	1.25(4)
N22	C22	1.35(1)
N22	C21	1.40(3)
C11	C21	1.52(1)

[a]Numbers in parentheses are e.s.d.s in the last significant digits.

TABLE 4. Selected bond angles (°) for [Pt(bpm)(CN)$_2$]·DMF [a]

Atom 1	Atom 2	Atom 3	Angle
N11	Pt	N21	79.0(3)
N11	Pt	C1	95.9(4)
N21	Pt	C2	97.4(4)
C1	Pt	C2	87.7(4)
Pt	C1	N1	178.6(10)
Pt	C2	N2	178.2(9)
Pt	N11	C11	116.8(7)
N11	C11	N12	127.3(9)
C11	N12	C12	116.1(13)
N12	C12	C13	122.7(11)
C12	C13	C14	117.4(14)
C13	C14	N11	121.3(12)
C14	N11	Pt	127.9(7)
C14	N11	C11	115.3(8)
Pt	N21	C21	115.1(6)
N21	C21	N22	122.5(9)
C21	N22	C22	114.8(12)
N22	C22	C23	123.4(10)
C22	C23	C24	121.5(14)
C23	C24	N21	118.0(12)
C24	N21	Pt	125.0(7)
C24	N21	C21	119.9(8)
N11	C11	C21	113.9(9)
N12	C11	C21	118.8(9)
N21	C21	C11	115.2(8)
N22	C21	C11	122.4(9)

[a]Numbers in parentheses are e.s.d.s in the last significant digits.

atoms in the complex is the same as used in ref. 11. N3, C3, C4 are atoms of the DMF molecule. In each complex the platinum atom and its surrounding form a plane arrangement of point symmetry C_{2v} (double group C'_{2v}). The complexes are stacked along the crystallographic b axis (= needle axis), yielding parallel zigzag chains of platinum atoms with an intra chain Pt–Pt distance of 3.2839(2) Å, cf. Fig. 2. Neighboring complexes of a chain are mutually rotated by 180°. The planes of the complexes are inclined to the crystallographic ac plane by an angle of 8°.

Spectroscopy

Figure 3 shows the polarized absorption spectra of single crystal [Pt(bpm)(CN)$_2$]·DMF (thickness ~20 μm) at T = 10 K and 295 K, respectively. At T = 10 K the E⊥b polarized spectrum exhibits one absorption band (maximum at $\bar{\nu}$ = 18 100 ± 50 cm^{-1},

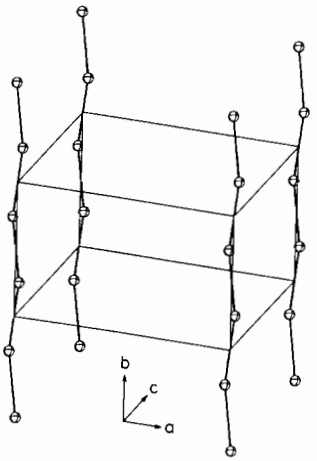

Fig. 2. Chain structure formed by the platinum atoms in single crystal [Pt(bpm)(CN)$_2$]·DMF.

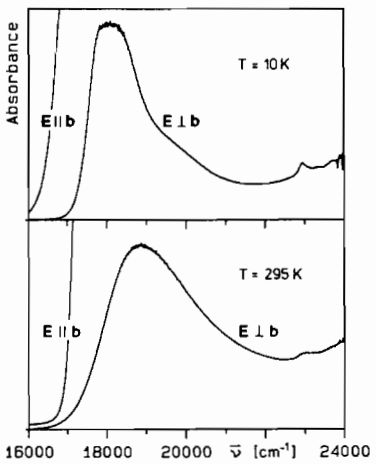

Fig. 3. Polarized absorption spectra of single crystal [Pt-(bpm)(CN)$_2$]·DMF at T = 10 K and 295 K, respectively. Thickness of the crystal about 20 μm.

$\epsilon_\perp \lesssim 200\ M^{-1}\ cm^{-1}$, half width $\Delta\bar{\nu}_{1/2} \sim 1500\ cm^{-1}$) with a weak shoulder at $\bar{\nu} \sim 19\,500\ cm^{-1}$. From the strong **E∥b** absorption only the low energy edge (at $\bar{\nu} \sim 16\,250\ cm^{-1}$) could be determined. Increase of the temperature from $T = 10$ K to 100 K and to room temperature shifts the **E⊥b** band by $\Delta\bar{\nu} \sim 180$ and $\sim 900\ cm^{-1}$, respectively, to the blue and broadens the half-width to $\bar{\nu}_{1/2} \sim 2500\ cm^{-1}$. The extinction is slightly lowered. The red flank of the **E∥b** absorption is also blue shifted.

The luminescence spectrum of single crystal $[Pt(bpm)(CN)_2]\cdot DMF$ at $T = 1.9$ K is composed of two broad bands with **E⊥b** and **E∥b** polarization, respectively, cf. Fig. 4. The corresponding energies of the maxima and the half-widths are $\bar{\nu}_\perp = 14\,660 \pm 20\ cm^{-1}$, $\bar{\nu}_\parallel = 15\,770 \pm 20\ cm^{-1}$, and $\Delta\bar{\nu}^\perp_{1/2} \sim 1100\ cm^{-1}$, $\Delta\bar{\nu}^\parallel_{1/2} \sim 980\ cm^{-1}$, respectively. Increase of the temperature influences distinctly the spectral positions, the intensities, and the half-widths of the emission bands. Between $T = 1.9$ and 7 K the **E⊥b** band is blue shifted by $\Delta\bar{\nu}_T = 250 \pm 20\ cm^{-1}$, as shown in Fig. 5. Further temperature increase to $T =$ 30 K yields no change of the spectral position, at $T > 30$ K, however, an additional blue shift occurs reaching a total value of $\Delta\bar{\nu} = 1300\ cm^{-1}$ at room temperature. The energy of the **E∥b** band maximum is nearly constant between $T = 1.9$ K and 30 K. At $T > 30$ K the **E∥b** band shows the same blue shift with increasing temperature as the **E⊥b** band.

The intensity $I_\perp$ of the **E⊥b** band grows by a factor of about 10 between $T = 1.9$ and ~ 7 K, cf. Fig. 6. At further increase of temperature the **E⊥b** intensity is strongly reduced, and at $T \sim 150$ K it reaches a value nearly twice as large as that at $T = 1.9$ K. Within

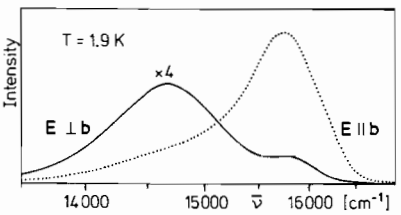

Fig. 4. Polarized emission spectra of single crystal $[Pt(bpm)(CN)_2]\cdot DMF$ at $T = 1.9$ K. $\lambda_{exc} = 364$ nm.

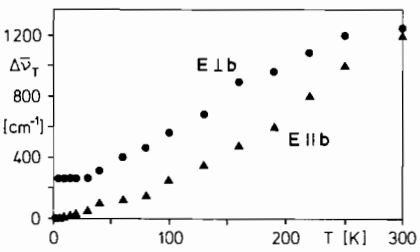

Fig. 5. Blue shift $\Delta\bar{\nu}_T$ of the emission maxima of single crystal $[Pt(bpm)(CN)_2]\cdot DMF$ for E⊥b and E∥b polarization, respectively, as functions of temperature. $\lambda_{exc} = 364$ nm.

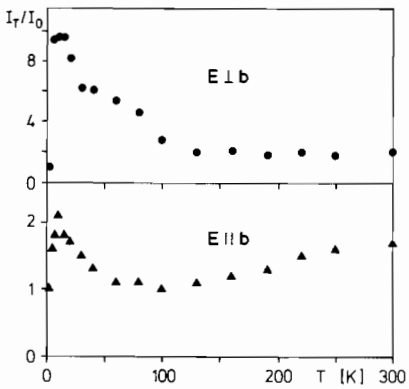

Fig. 6. Relative emission intensities I_T/I_0 of single crystal $[Pt(bpm)(CN)_2]\cdot DMF$ for E⊥b and E∥b polarization, respectively, as functions of temperature. $\lambda_{exc} = 364$ nm.

the range $150\ K \lesssim T \lesssim 295$ K the **E⊥b** intensity remains constant. The **E∥b** emission exhibits a qualitatively similar behavior, however, the intensity $I_\parallel$ increases between $T = 1.9$ and ~ 10 K by a factor of only 2, and at $T > 150$ K a weak temperature induced enhancement of the **E∥b** intensity is observed. Correspondingly the intensity ratio $I_\parallel/I_\perp$ as a function of the temperature shows a drastic decrease between $T = 1.9$ and ~ 7 K. With increasing temperature the ratio grows, and at room temperature it reaches nearly its low temperature value. The half-width of both the **E⊥b** and **E∥b** band is broadened by a factor of about 2 between $T = 1.9$ K and room temperature.

In the temperature range $1.9\ K \leqslant T \leqslant 295$ K the decay curves of the **E⊥b** emission are monoexponential and the lifetime varies between $\tau = 1800$ and 0.1 μs. Between $T = 1.9$ and 15 K the lifetime of the **E⊥b** emission is lowered by a factor of about 100. The corresponding values of the **E∥b** emission are shorter than 3 ns.

Magnetic fields **H** affect the emission of single crystal $[Pt(bpm)(CN)_2]\cdot DMF$ at $T = 1.9$ K, provided **H** is perpendicular to the crystallographic *b* axis, **H⊥b**. Changes of the emission properties have been found only for the **E⊥b** polarized component. Its maximum is blue shifted by $\Delta\bar{\nu}_H = 220\ cm^{-1}$, if the field strength H is increased from $H = 0$ to 1.2 T, cf. Fig. 7. Further increase of H yields no additional shift. Between $H = 0$ and 6 T the **E⊥b** intensity $I_\perp$ is enhanced by a factor of 27. At $H \lesssim 2$ T the dependence of $I_\perp$ on the field strength H can be described by the relation $I_\perp(H) - I_\perp(0) \sim H^2$. The half-width of the **E⊥b** band is reduced from $\Delta\bar{\nu}^\perp_{1/2} = 1100\ cm^{-1}$ to $830\ cm^{-1}$, if the field strength is increased from $H = 0$ to 6 T. Drastic magnetic field effects have been observed for the lifetime of the **E⊥b** polarized emission at $T = 1.9$ K. By a magnetic field **H⊥b** of strength $H = 6$ T it is reduced from $\tau = 1.8$ ms to 15 μs. The

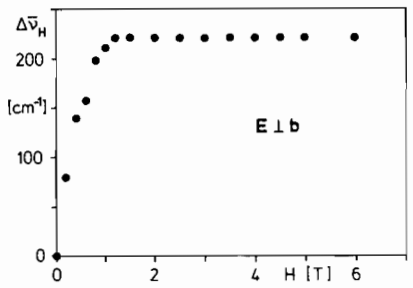

Fig. 7. Energy shift $\Delta\bar{\nu}_H$ of the maximum of the E⊥b polarized emission of single crystal $[Pt(bpm)(CN)_2]\cdot DMF$ as a function of the magnetic field strength H at $T = 1.9$ K. H⊥b. $\lambda_{exc} = 364$ nm.

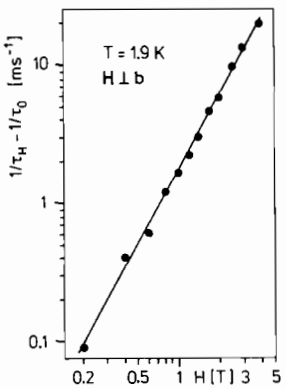

Fig. 8. Change of the deactivation rate, $1/\tau_H - 1/\tau_{H=0}$, of single crystal $[Pt(bpm)(CN)_2]\cdot DMF$ as a function of the magnetic field strength H at $T = 1.9$ K. H⊥b. $\lambda_{exc} = 364$ nm.

decay is mono-exponential in the whole range $0 \leqslant H \leqslant 6$ T. A log–log plot of $1/\tau_H - 1/\tau_{H=0}$ versus H yields a straight line, as shown in Fig. 8. Its slope has a value of ~ 1.9, indicating that $1/\tau_H - 1/\tau_{H=0}$ is nearly a purely quadratic function of H.

At $T > 5$ K no magnetic field effects on the emission properties of single crystal $[Pt(bpm)(CN)_2]\cdot DMF$ were found.

Discussion

The electronic structure of the single complex $[Pt(bpm)(CN)_2]$ has been discussed comprehensively in ref. 11. The HOMO of the complex transforms according to a_2 (symmetry group C_{2v}) and is a hybrid of the metal 5d-state $a_2(xy)$ and the bpm state $a_2(\pi_{bpm})$. For the LUMO a mixture of the metal 6p-state $b_1(x)$ and the ligand states $b_1(\pi^*_{CN})$ and $b_1(\pi^*_{bpm})$ is expected. Thus, the complex has the ground electronic state $^1A_1(A_1')$ and the lowest excited electronic states $^3B_2(A_1', A_2', B_1')$ and $^1B_2(B_2')$. The primed symbols label the spin–orbit components according to the double group C'_{2v}. These states are preserved nearly also in the crystal inasmuch as the complexes do not interact distinctly. The interaction will be small, if the inter-complex distance is sufficiently large. This case is realized for the $[Pt(bpm)(CN)_2]\cdot H_2O$ crystal, with the shortest Pt–Pt distance R of 3.435 Å. In single crystal $[Pt(bpm)(CN)_2]\cdot DMF$, however, a distinctly shorter Pt–Pt distance ($R \sim 3.28$ Å) has been observed and neighboring complexes of a column have nearly face-to-face arrangement (except the mutual 180° rotation of the complexes), as shown in Figs. 1 and 2.

For single crystal $[Pt(bpm)(CN)_2]\cdot DMF$ the relatively short intra-columnar Pt–Pt distance indicates an interaction between neighboring complexes, mainly through orbitals with large extension along the b axis. This property is expected for the LUMO $b_1(x, \pi^*_{CN}, \pi^*_{bpm})$ which forms the conduction band of the crystal. The HOMOs $a_2(xy, \pi_{bpm})$ of neighboring complexes will yield only a weak overlap and, thus, the resulting band will be small. The metal orbitals $a_1(x^2)$, however, direct their maximum extension towards the neighboring platinum atoms, and the upper edge of the corresponding broad band will have an energy higher than the small a_2 band due to the HOMOs. Thus, the ground electronic state is a singlet $^1A_1(A_1')$ and the first excited electronic bands of the crystal have, unlike the single complex, the symmetry $^1B_1(B_1')$ and $^3B_1(A_1', A_2', B_2')$, respectively. The left hand side of Fig. 9 shows schematically the lower edges of the excited bands of $^1B_1$ and $^3B_1$ parentage. The energy order of the triplet components, $A_2' < A_1' \sim B_2'$, has been chosen according to the experimental results, as will be shown below. From symmetry selection rules it follows that the transitions A_1', $B_2'(^3B_1) \leftrightarrow A_1'(^1A_1)$ and $B_1'(^1B_1) \leftrightarrow A_1'(^1A_1)$ are electric dipole allowed with E⊥b and E∥b polarization, respectively, whereas the low energy transition $A_2'(^3B_1) \leftrightarrow (^1A_1)$ is only vibronically allowed (E⊥b polarization with α_2 or β_1 vibrations).

The weak E⊥b polarized and the strong E∥b polarized absorption can be assigned to the spin forbidden transition $A_1'(^1A_1) \rightarrow A_1'$, $B_2'(^3B_1)$ and to the full allowed transition $A_1'(^1A_1) \rightarrow B_1'(^1B_1)$, respec-

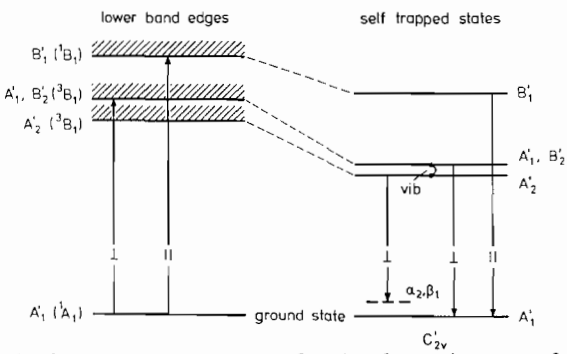

Fig. 9. Energy level diagrams for the electronic states of a $[Pt(bpm)(CN)_2]$ chain; left-hand side: lower band edges; right-hand side: self-trapped states.

tively. The temperature induced blue shift of the **E⊥b** absorption band and of the red flank of the **E∥b** absorption are due to the thermal increase of the intra-columnar Pt–Pt distances yielding a reduction of the electronic band widths and, thus, an increase of the energy gap between the ground state and the lower band edges.

The emission spectra can be traced back to the radiative deactivation of states, whose energy is lower than that of the corresponding electronic bands, cf. the right hand side of Fig. 9. The stabilization of these states is probably due to self trap mechanism. At $T = 1.9$ K the **E⊥b** polarized emission (maximum at $\bar{\nu}_\perp = 14\,660$ cm^{-1}) originates from the vibronic transition $A_2'(^3B_1) \rightarrow A_1'(^1A_1) + \alpha_2,\beta_1$ whereas the **E∥b** polarized emission (maximum at $\bar{\nu}_\parallel = 15\,770$ cm^{-1}) can be assigned to the fluorescence transition $B_1'(^1B_1) \rightarrow A_1'(^1A_1)$, which is fully allowed already at low temperatures. The weak emissions at ~14 600 (**E∥b**) and at ~15 800 (**E⊥b**) cm^{-1} are caused probably by several factors. Both are partly due to the inclination of the complex planes to the crystallographic *ac* plane (~8°) and to depolarization effects of the cryostat windows. A contribution to the weak **E∥b** emission at ~14 600 cm^{-1} can also be owing to a vibronic transition $A_2'(^3B_1) \rightarrow A_1'(^1A_1) + \beta_2$. With increasing temperature the states $A_1'(^3B_1)$ and $B_2'(^3B_1)$ become thermally populated. Since the radiative deactivation of these states to the ground electronic state is directly (without the assistance of a vibration) allowed, an additional emission channel is opened, which is blue shifted by $\Delta\bar{\nu}_\perp = \Delta E + \bar{\nu}_{vib}$, with ΔE the energy distance between $A_2'(^3B_1)$ and the pair of triplet components A_1', B_2'. $\bar{\nu}_{vib}$ denotes one quantum of a vibration, used for the vibronic transition $A_2' \rightarrow A_1'$. The blue shift of $\Delta\bar{\nu}_T = 250$ cm^{-1}, observed at increase of the temperature from $T = 1.9$ K to 7 K (cf. Fig. 5), is a lower limit of $\Delta\bar{\nu}_\perp$. The temperature dependence of the emission lifetime and of the intensity, cf. Fig. 6, confirms the above assignment and yields for ΔE a value of about 25 cm^{-1}.

The additional blue shift of the emission (**E⊥b** and **E∥b** polarization) between $T \sim 30$ K and room temperature can be traced back to the thermal expansion of the intra-columnar Pt–Pt distances. The decrease of the emission lifetime and of the emission intensity at higher temperatures is due to an enhancement of non-radiative deactivations.

The effects of applied magnetic fields can be understood by arguments based on perturbation theory [1, 4]. A magnetic field **H⊥b** lowers the symmetry C_{2v}' to C_2' for **H∥z** or to C_s' for **H∥y**. In both cases the lowest excited state $A_2'(^3B_1)$ gets an admixture of the pair of states A_1', $B_2'(^3B_1)$, and thus the direct electronic transition $A_2'(^3B_1) \rightarrow A_1'(^1A_1)$ with **E⊥b** polarization becomes partly allowed. The energy of this transition is higher by $\bar{\nu}_{vib}$ than that of the corresponding vibronic desactivation of the state A_2' at $H = 0$. With increasing field strength H the above mentioned admixture increases and at low temperature the blue shifted **E⊥b** emission acquires intensity by this mechanism. That both the intensity and the change of the radiative deactivation rate, cf. Fig. 8, are nearly purely quadratic functions of the magnetic field strength, is in agreement with the results of quantum mechanical perturbation theory.

Supplementary Material

Tables containing values of F_0 and F_c, anisotropic thermal parameters, and a complete list of atomic distances and bond angles can be obtained upon request from the authors.

Acknowledgements

We would like to thank the Fonds der Chemischen Industrie and the Deutsche Forschungsgemeinschaft for support of our work.

References

1 G. Gliemann and H. Yersin, *Struct. Bonding (Berlin), 62* (1985) 87.
2 W. Holzapfel, H. Yersin and G. Gliemann, *Z. Kristallogr., 47* (1981) 157.
3 G. Gliemann, *Commun. Inorg. Chem., 5* (1986) 263.
4 I. Hidvegi, W. v. Ammon and G. Gliemann, *J. Chem. Phys., 76* (1982) 4361; W. v. Ammon, I. Hidvegi and G. Gliemann, *J. Chem. Phys., 80* (1984) 2837.
5 R. Dillinger, G. Gliemann, H. P. Pfleger and K. Krogmann, *Inorg. Chem., 22* (1983) 1366.
6 J. Biedermann, M. Wallfahrer and G. Gliemann, *J. of Lumin., 37* (1987) 323.
7 R. Schwarz, M. Lindner and G. Gliemann, *Ber. Bunsenges. Phys. Chem., 91* (1987) 1233.
8 R. Schwarz and G. Gliemann, *Z. Naturforsch., Teil A, 44* (1989) 99.
9 P. M. Kiernan and A. Ludi, *J. Chem. Soc., Dalton Trans.*, (1978) 1127.
10 W. Tuszynski and G. Gliemann, *Ber. Bunsenges. Phys. Chem., 89* (1985) 940.
11 J. Biedermann, G. Gliemann, U. Klement, K.-J. Range and M. Zabel, *Inorg. Chim. Acta, 169* (1989) 63.